






## Article

# Two-Point Resolution of a Defocused Imaging System Based on Spatially Coherent Illumination

Gianlorenzo Massaro <sup>1,2,\*</sup> , Sergio de Gioia <sup>1,2</sup> , Adalberto Brunetti <sup>1</sup> , Francesco V. Pepe <sup>1,2</sup>   
and Milena D'Angelo <sup>1,2</sup> 

<sup>1</sup> Dipartimento di Fisica, Università degli Studi di Bari, 70125 Bari, Italy; sergio.degioia@uniba.it (S.d.G.); francesco.pepe@ba.infn.it (F.V.P.); milena.dangelo@uniba.it (M.D.)

<sup>2</sup> Istituto Nazionale di Fisica Nucleare, Sezione di Bari, 70125 Bari, Italy

\* Correspondence: gianlorenzo.massaro@uniba.it

**Abstract:** We examine the physical limitations and performance of spatially coherent imaging systems under defocused conditions using a modified two-point resolution criterion. By comparing coherent and incoherent illumination regimes, in defocused conditions, we highlight the peculiar advantages of coherent systems in resolving closely spaced features while maintaining a high depth of field. The analysis identifies two primary contributions to image degradation in coherent defocused systems: image broadening and interference-related contrast reduction. Through a specifically designed analytical framework, this study confirms that resolution degradation in coherent imaging is characterized by a square root dependence on defocusing distance, irrespective of the numerical aperture. This behavior starkly contrasts with incoherent imaging, where the resolution deteriorates linearly with defocusing and exhibits a strong dependence on the system's numerical aperture. Furthermore, we provide explicit analytical expressions for contrast loss and minimum resolvable object size under defocused coherent conditions, offering deeper insights into their relation with system parameters. These results corroborate the superior performance of coherent imaging in resolving fine details in defocused environments, challenging conventional optical paradigms. Our findings not only extend the theoretical understanding of coherent imaging but also establish practical guidelines to optimize optical systems for high-resolution applications.



**Citation:** Massaro, G.; de Gioia, S.; Brunetti, A.; Pepe, F.V.; D'Angelo, M. Two-Point Resolution of a Defocused Imaging System Based on Spatially Coherent Illumination. *Photonics* **2024**, *11*, 1203. <https://doi.org/10.3390/photonics11121203>

Received: 26 November 2024

Revised: 14 December 2024

Accepted: 20 December 2024

Published: 22 December 2024



**Copyright:** © 2024 by the authors. Licensee MDPI, Basel, Switzerland. This article is an open access article distributed under the terms and conditions of the Creative Commons Attribution (CC BY) license (<https://creativecommons.org/licenses/by/4.0/>).

**Keywords:** coherent imaging; spatial coherence; optical resolution

## 1. Introduction

Quantum imaging is a rapidly evolving field that has significantly enriched the landscape of high-resolution imaging by exploiting both entanglement and classical correlations [1,2]. Techniques such as sub-shot-noise imaging [3,4], quantum lithography [5–7], and quantum-enhanced resolution [8–11] leverage *nonclassical* photon statistics to surpass classical limits. Quantum lithography, for instance, overcomes the limits of classical optics by utilizing entangled photon states to achieve patterns beyond the diffraction limit, paving the way for high-precision fabrication [7,12]. Advances in quantum-enhanced sensing have also introduced methods for imaging faint or weakly illuminated objects with high sensitivity, such as the use of squeezed states of light [13–15], enabling phase-sensitive detection [16,17]. One of the most known quantum imaging techniques is ghost imaging [18,19], using photon pairs or light beams to reconstruct images starting from a single-pixel detector, while demonstrating robustness against noise and scattering [20,21]. Ghost imaging holds particular significance for quantum imaging, as its study revealed that quantum imaging can be achieved not only through quantum entanglement but also using chaotic light correlations [22–29].

Recent progress in quantum and quantum-inspired unconventional imaging has opened new avenues for achieving high-resolution three-dimensional (3D) imaging through

the combined use of light intensity and photon correlations [30–33]. A key advancement of the correlation-based imaging approach, inspired by ghost imaging and named correlation plenoptic imaging (CPI) [30], is the capability of recovering object details, even when samples are placed well outside the natural depth of field defined by the numerical aperture of the imaging system (i.e., in *defocused* imaging conditions). CPI thus departs from conventional optical limitations. In fact, the CPI approach works in an extended axial range compared to incoherent imaging and is characterized by a resolution that does not depend on the numerical aperture (NA) of the imaging system [31,34].

This exceptional behavior of CPI has been found to stem from the spatial coherence of light [34–36]. The NA independence of the resolution of CPI is indeed in direct conflict with the well-known NA-dependent circle of confusion (CoC) responsible for image blurring in defocused incoherent imaging systems [37].

Interestingly, recent studies have demonstrated the possibility of achieving the same resolution versus depth of field performance of CPI in correlation-free schemes, provided spatially coherent illumination is employed and bright-field imaging is considered [38,39]. This result has been validated in transmission microscopy, where the use of an LED array synchronized with the microscope camera has been shown to enable the NA-independent resolution of several defocused transmissive samples (from test targets to bovine cornea and colored histological sections of mouse brains) with no need for photon correlation measurements [38]. Translating the optical performance of CPI outside of its original context of correlation-based imaging opens the door to a great simplification of the optical design, as well as to the possibility of performing volumetric imaging at a much higher signal-to-noise ratio [25,29,40–44]. The NA-independent volumetric imaging capability of both CPI and its correlation-free coherence-based counterpart is in contrast with traditional imaging systems favoring incoherent illumination, which excel in simplicity and real-time imaging for thin samples but falter with thick or defocused objects due to the NA-dependent and CoC-defined blurring and depth-of-field (DOF) [37,45–48]. Coherent illumination thus offers solutions to the well-known resolution–DOF trade-off of incoherent imaging systems, enabling one to achieve higher resolution for defocused samples.

Coherence has also been found to play a very relevant role in the recent innovation of Correlation Hyperspectral Imaging (CHI), where correlations are employed to capture high-resolution spectral and spatial information, overcoming traditional limitations in snapshot and scanning techniques [49].

Interestingly, until the developments reported in Ref. [38], bright-field light-field imaging with coherent light was employed to achieve improved resolution and DOF, but its adoption was limited to computationally intensive inverse imaging methods like holography and ptychography [50–59]. Fringing artifacts and incomplete theoretical frameworks have further restricted the broader use of coherent illumination in direct imaging [38,60,61]. The work reported in Ref. [38], on the other hand, has opened up the possibility of tailoring imaging systems to leverage spatial coherence while still working in the framework of direct imaging [36].

These developments redefine the role of spatial coherence as a deliberate tool for optical enhancement, pushing the boundaries of high-resolution imaging. However, the integration of spatial coherence into the analysis of defocused imaging systems requires moving beyond the typical mathematical tools employed to define resolution in incoherent imaging systems and adopting frameworks that fully exploit coherence-driven enhancements: traditional incoherent methodologies, such as the point-spread function and transfer function, can work well to describe perfectly focused coherent imaging systems [62] but need to be deeply modified in view of defining the resolution in the defocused coherent regime [38,39]. Only a formally correct analysis of nonlinear imaging formation, such as coherent imaging, can thus reveal the profound impact of the coherence of light on imaging performance while also providing new insights into the physical limits of coherent systems [31,38,39].

In the context of CPI, the resolution of defocused images was originally quantified by means of visibility (see, e.g., Refs. [31,63]); a more rigorous approach was proposed in Ref. [38], where the concept of image fidelity has enabled, for the first time, a direct comparison between the performance of defocused coherent and incoherent imaging. The analysis of the resolution of periodically patterned objects illuminated by spatially coherent light was also recently presented in Ref. [39].

In this work, for the first time, we extend the concept of two-point resolution to defocused coherent imaging systems. The so-called two-point resolution criterion, giving the minimum separation between two points resulting in a resolved image, is in fact a widely used criterion for estimating the imaging performance of incoherent imaging systems and is widely used both in standard imaging configurations [64,65] and in quantum architectures, such as ghost imaging [66]. Its extension to *focused* coherent imaging systems is also well known (see, e.g., [62,67]) and does not require the introduction of dedicated mathematical tools. On the contrary, as we shall demonstrate here, its naive extensions to defocused coherent imaging leads to non-physical results. To address this challenge, we introduce parametric *resolution* curves based on a contrast criterion. As we shall see, the proper and physically sound extension of two-point resolution to defocused coherent imaging requires taking into proper account the profound physical differences between coherent and incoherent imaging, such as interference phenomena.

This paper is organized as follows. We first compare image formation under coherent and incoherent illumination by using a two-slit object; this enables us to show that incoherent images are simple superpositions of the intensity from the two slits, both in focused and in defocused conditions, while defocused coherent images include interference terms. Unlike the well-known case of *focused* coherent imaging where the degradation of the image quality outside of the focused plane is attributed, in the case of coherent illumination, degradation is attributed to two factors: slit image broadening and interference-induced contrast loss. At first, we present a naive model of two-point resolution, based on the assumption of vanishing slit aperture, along the line of the point-spread function employed for characterizing incoherent imaging; this approach is found to inaccurately attribute the degradation of the contrast to geometric optics, which is in contrast with the diffractive nature of coherent defocusing (as discussed in detail in Ref. [38]). We thus introduce a more rigorous two-point resolution method, which ties the slit size and separation; this approach leads us to find, for a fixed contrast threshold, the expected square root scaling of the image size with the defocusing, which was discovered and demonstrated, both theoretically and experimentally, in Refs. [36,38,39]. The presented analytical expression for the contrast-based resolution limit under defocusing conditions further confirms that the degradation of contrast is equally shared between the two identified contributions: the broadening of the light distribution forms each slit and the interference of coherent light passing through the two slits. This paper thus proposes both a new tool for analyzing defocused coherent imaging systems and offers new insights about the physics behind the enhanced performances of coherent over incoherent imaging systems in the defocused imaging regime.

## 2. Materials and Methods

### 2.1. Coherent Optical Response of Single-Lens Defocused Imaging System to Two-Slit Object

Let us consider an object with transverse field transmittance  $A(x_0)$ , with  $x_0$  being the transverse spatial coordinate in the plane of the sample. Without loss of generality, we shall simplify the notation by limiting the calculations to only one coordinate ( $x$ ) in the transverse plane. The image obtained by observing this object through an imaging device illuminated by spatially coherent light is given by

$$I_{\text{coh}}(x; \delta) = \left| \int A(x_0) g_{\delta}(x_0, x) dx_0 \right|^2, \quad (1)$$

where  $g_\delta(x_0, x)$  is the Green's function propagating the electric field from the sample plane to the detection plane, with  $x$  being the transverse coordinate in the detector plane. The Green's function depends on a parameter  $\delta$  that describes the *defocusing* of the sample, namely how far from focus the sample is placed.

For comparison, the image of a sample obtained with *incoherent* illumination, observed through the same optical design, is given by the expression

$$I_{\text{inc}}(x; \delta) = \int |A(x_0)|^2 |g_\delta(x_0, x)|^2 dx_0. \tag{2}$$

The linearity of Equation (2) makes it so that the optical performance of an incoherent imaging system can be assessed with the conventional methods used for linear imaging systems, such as the point-spread function (PSF), modulation transfer function, knife edge, or two-point resolution. This paper will focus on the last criterion, showing that the absence of the PSF, for coherent imaging systems, imposes significant challenges to the study of a generalized two-point resolution criterion [39].

To show the differences, let us consider a transmissive object mask made of two Gaussian slits, namely

$$A^-(x_0; \sigma, d) + A^+(x_0; \sigma, d) = \begin{cases} A(x_0) & \text{for a coherent system,} \\ |A(x_0)|^2 & \text{for an incoherent system,} \end{cases} \tag{3}$$

where

$$A^\pm(x_0; \sigma, d) = \exp\left[-\frac{(x_0 \mp d/2)^2}{2\sigma^2}\right]. \tag{4}$$

Notice that the given definition takes into account the sensitivity of coherent systems to the field transmittance and of incoherent systems to the transmitted intensity. By plugging (3) into (2), we see that, as is well known for linear imaging systems, the image of a double-slit object results in the superposition of the two images of each slit:

$$I_{\text{inc}}(x; \delta, \sigma, d) = I_{\text{inc}}^+(x; \delta, \sigma, d) + I_{\text{inc}}^-(x; \delta, \sigma, d), \tag{5}$$

where

$$I_{\text{inc}}^\pm(x; \delta, \sigma, d) = \int A^\pm(x_0; \sigma, d) |g_\delta(x_0, x)|^2 dx_0 \tag{6}$$

is the incoherent image of a single slit centered in  $d/2$ . The case of coherent imaging is very different, since

$$I_{\text{coh}}(x; \delta, \sigma, d) = I_{\text{coh}}^+(x; \delta, \sigma, d) + I_{\text{coh}}^-(x; \delta, \sigma, d) + 2\text{Re}\Phi(x; \delta, \sigma, d), \tag{7}$$

where

$$I_{\text{coh}}^\pm(x; \delta, \sigma, d) = \left| \int A^\pm(x_0; \sigma, d) g_\delta(x_0, x) dx_0 \right|^2 \tag{8}$$

are the coherent images of the two slits, taken separately, and

$$\Phi(x; \delta, \sigma, d) = \int \int A^+(x_0; \sigma, d) A^-(x'_0; \sigma, d) g_\delta(x_0, x) g_\delta^*(x'_0, x) dx_0 dx'_0 \tag{9}$$

is a complex interference term, describing the contribution to the image from the overlap of the contributions from the two slits. As can be seen by a comparison of Equations (5) and (7), this term is responsible for the deep difference between coherent and incoherent imaging systems and stems from the nonlinearity of the former.

In the case of a single object, the difference between the imaging performance of the two systems is obtained by comparing the two terms  $I_{\text{inc}}^\pm$  and  $I_{\text{coh}}^\pm$  taken separately; this analysis was already conducted in Ref. [38], where it was shown that, for any given defocusing offset, the resolution is higher in the coherent imaging regime than in the

incoherent one and degrades with increasing defocusing with an NA-independent square root scaling in the coherent case and with an NA-dependent linear trend in the incoherent case. Of course, such results are independent of the transverse displacement  $d/2$ , provided the system is paraxial, as we shall assume throughout the entire paper.

From now on, we shall assume that the pupil(s) involved in the setup has(have) Gaussian apodization, namely, the complex PSF of the system is Gaussian. For definiteness, we shall assume, without loss of generality, that the imaging system is a single-lens design with unit magnification (i.e., object distance is equal to image distance). In this case, the complex PSF is given, within a scale factor, by

$$\int_{-\infty}^{\infty} \exp \left[ i \frac{k}{2(o+\delta)} (x_0 - x_l)^2 - i \frac{k}{o} x_l^2 - \frac{x_l^2}{4\sigma_l^2} + i \frac{k}{2o} (x_l - x)^2 \right] dx_l, \quad (10)$$

where the integration variable  $x_l$  is the coordinate in lens plane,  $k$  is the wavenumber of the illumination light, and the four terms in the exponential are due, respectively, to:

- Free-space paraxial propagation of the field traveling a distance  $o + \delta$  from the object, with  $o$  being the distance between the focus plane and the lens and  $\delta$  the axial offset of the object relative to the focus plane position.
- Phase and amplitude contributions of the propagation through a thin lens of focal length  $o/2$ , with  $\sigma_l$  representing the extent of the lens aperture opening accounting for the Gaussian apodization.
- Free-space paraxial propagation from the lens to the detector plane over the distance  $o$ .

Since the system has a Gaussian response function, the three terms contributing to Equation (7) have the form

$$I_{\text{coh}}^+(x; \delta, \sigma, d) \simeq \exp \left[ -\frac{(x - M(\delta)d/2)^2}{\sigma_{\text{coh}}^2(\delta, \sigma, d)} \right] = \exp \left[ -\frac{(x - M(\delta)d/2)^2}{\sigma_{\text{coh}}^2(\delta, \sigma)} \right], \quad (11)$$

$$I_{\text{coh}}^-(x; \delta, \sigma, d) = I_{\text{coh}}^+(x; \delta, \sigma, -d) \quad (12)$$

$$\text{Re}\Phi(x; \delta, \sigma, d) = \exp \left[ -\frac{d^2}{2\phi^2(\delta, \sigma)} - \frac{x^2}{\sigma_{\text{cross}}^2(\delta, \sigma)} \right] \cos[\kappa(\delta, \sigma, d)x], \quad (13)$$

as reported in the left panel of Figure 1 (see Appendix A for the analytical expression of  $\sigma_{\text{coh}}$ ,  $\phi$ ,  $\sigma_{\text{cross}}$ , and  $\kappa$ ). Hence,

- The first two terms correspond to the coherent images of the two slits considered separately. The second approximate equality stems from the fact that the width of the images  $\sigma_{\text{coh}}$  has a very weak dependence on the transverse displacement on the optical axis  $d/2$  so that, in paraxial conditions ( $d \ll o$ ), it can be neglected. In this case, the image  $I_{\text{coh}}^+$  corresponds exactly to the image of a slit on the optical axis (the case treated in [38]), displaced by a quantity  $M(\delta)\frac{d}{2} = \frac{o}{o+\delta}\frac{d}{2}$ .
- The last term, corresponding to the interference between the two slits, is even in the spatial coordinate  $x$  and can be thought of as three separate factors. The first factor does not depend on  $x$  and regulates the amplitude of the interference term; it is increasingly less relevant as the distance between the slits is increased. The second term is a Gaussian envelope, whose width does not depend on the slit distance but only on the width. The last contribution is an oscillating term, whose spatial period depends on all parameters into play.

From an analysis of the analytical expressions of the quantities defined above, one finds out that the phenomena contributing to the degradation of the image quality in the parameter space  $(\delta, \sigma, d)$  are two. Firstly, one finds that  $\sigma_{\text{coh}} > \sigma$ , namely, the coherent image of a single slit, is always larger than the original slit, except for the focused case ( $\delta = 0$ ) and infinite numerical aperture, in which case  $\sigma_{\text{coh}} \rightarrow \sigma$ . This case is well known and accounted for, as is analyzed in [38]. Another contribution to the worsening of the image

quality, however, is the fact that the final image can show an undesired local maximum on the origin, whose height is defined by the argument of the first Gaussian term in its expression. In fact, due to the Gaussian envelope that modulates the oscillating term, the main disturbance to the image quality is expected to be given by the absolute maximum of the function, which, as we said, is in  $x = 0$ ; this is in line with the plot reported in the right panel of Figure 1.

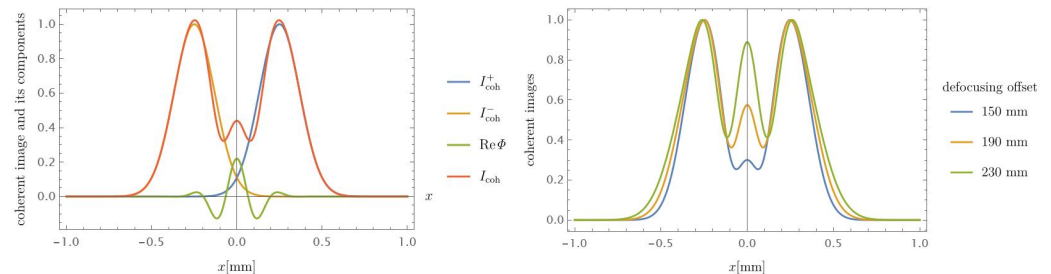


**Figure 1.** The left panel reports the theoretical intensity distribution in a coherent image and its composing parts [as identified in Equation (7)], in the case of an object mask made of two Gaussian slits with width  $\sigma = 0.1$  mm and center-to-center separation  $d = 0.5$  mm, placed at a defocusing distance  $\delta = 170$  mm. The right panel shows the behavior of the intensity distribution in the same conditions but for increasing values of defocusing; broadening and interference are found to be more pronounced. Images in both plots are normalized to the intensity maximum of a single slit, and employed wavelength is 500 nm.

Let us now study how the two concurring contributions to image degradation evolve in the parameter space.

### 2.2. Naive Coherent-regime Analogous of the Two-Point Resolution

As we have anticipated, if one analyzes the performance of a coherent image in terms of a two-point resolution, in the same way as it is performed with incoherent imaging systems, non-physical results are obtained. To show this, let us consider a “point-like” (PL) object, which in our formalism is obtained by considering

$$I_{coh}^{(PL)}(x; \delta, d) = \lim_{\sigma \rightarrow 0} I_{coh}(x; \delta, \sigma, d). \tag{14}$$

In this limit, the width of a coherent image (Equation (11)) is given by

$$\sigma_{coh}^{(PL)}(\delta) = \sqrt{\frac{1}{2}\sigma_{Rayleigh}^2 + \sigma_{CoC}^2(\delta)}, \tag{15}$$

where the first term

$$\sigma_{Rayleigh} = \frac{o}{k\sigma_l} \tag{16}$$

can be immediately recognized as the radius of the Airy disk, which gives the ultimate limit to the resolution of the system, and the second term

$$\sigma_{CoC} = 2 \frac{|\delta|\sigma_l}{o + \delta} \tag{17}$$

is the well-known circle of confusion (CoC). This result is in net contrast with very recent findings about the performance of coherent imaging systems, which demonstrate that the defocused performance of coherent imaging is not affected by any effect related to geometrical optics and is independent of the numerical aperture. Moreover, as expected, the width of the image of a slit is independent of  $d$ .

Similar results are also obtained by investigating the other mechanism of image degradation, namely the appearance of a local maximum on the origin. The relevance of

this contribution can be evaluated, for instance, as the *contrast* between the local maxima in the image of a single slit and the local maximum in the interference term, namely,

$$C^{(PL)}(\delta, d) = \frac{I_{\text{coh}}^+(x = M(\delta)\frac{d}{2}; \delta, \sigma \rightarrow 0, d)}{2\text{Re}\Phi(x = 0; \delta, \sigma \rightarrow 0, d)} = \frac{1}{2} \exp\left[\frac{d^2}{2(\phi^{(PL)}(\delta))^2}\right], \quad (18)$$

with

$$\phi^{(PL)}(\delta) = \sqrt{\sigma_{\text{Rayleigh}}^2 + \sigma_{\text{CoC}}^2(\delta)}. \quad (19)$$

This expression is quite interesting as it clearly predicts a correct qualitative behavior of the system: for increasing slit separations, the contrast between the absolute and relative maxima becomes increasingly large, thus leading to the prediction of a well-resolved image for large separation, as expected. However, the scaling constant regulating how quickly the image worsens for small values of  $d$  is again entirely geometrical, in perfect accordance with the previous result, but in net contrast with experimental evidence.

We shall now show that these misleading results have their common origin in the fact that the limiting case of  $\sigma \rightarrow 0$  does not really hold any physical meaning in the case of coherent imaging.

### 3. Results: True Coherent-regime Analogous of the Two-Point Resolution

Since the limit of  $\sigma \rightarrow 0$  does not give any meaningful results, we shall now study the case of small slits by bonding the slit size to the distance between the slits. Specifically, we shall assume  $\sigma = d/c$ , where  $c$  can be an arbitrarily large positive number, but not infinity. By fixing a value of  $c$ , the behavior of a coherent image can again be studied in the  $(\delta, d)$  parameter space, with the slit width becoming smaller as the values of  $d$  are decreased.

In these conditions, the behavior of the coherent image of the two slits, taken separately [Equation (11)], was studied in great detail in Ref. [38]. In that work, it was found that outside of the natural depth of field of the imaging device ( $|\delta| > 1/(k\text{NA}^2)$ ), the broadening of the Gaussian image ( $\sigma_{\text{coh}}(\delta, d/c)$ ) is accurately predicted in the infinite NA approximation by

$$\sigma_{\text{coh}}^{(\infty)}(\delta, d/c) = \lim_{\sigma_l \rightarrow \infty} \sigma_{\text{coh}}(\delta, d/c) = \sqrt{\left(\frac{d}{c}\right)^2 + \sigma_{\text{diff}}^2(\delta, d/c);} \quad (20)$$

where

$$\sigma_{\text{diff}} = \frac{c|\delta|}{kd}. \quad (21)$$

In fact, the image of a single Gaussian slit is enlarged by the contribution due to the diffraction toward the plane in focus, with its characteristic direct proportionality to the propagation distance and inverse proportionality to the slit width.

By analogy, we now study the other origin of the image degradation as the contrast between the maxima:

$$C(\delta, d; c) = \frac{1}{2} \exp\left[-\frac{d^2}{2\phi^2(\delta, d/c)}\right]. \quad (22)$$

The analytical expression of this term is cumbersome and shall not be reported here; however, Figure 2 reports the plot highlighting this region in the parameter space  $(\delta, d)$ . The colored part of the plot indicates the area corresponding to a contrast value larger than an arbitrarily chosen threshold value. As can be immediately recognized, the limit to the contrast area is very similar to the square root trend shown in Ref. [38] for the case of a single Gaussian slit; this hints that also image degradation due to the loss of contrast between the two maxima might be regulated by the same physical scaling demonstrated

in Ref. [38] for the degradation due to slit width. To show that this is the case, we shall consider the infinite NA limit for the contrast:

$$C^{(\infty)}(\delta, d; c) = \lim_{\sigma_1 \rightarrow \infty} C(\delta, d; c), \tag{23}$$

and then consider the parametric curves

$$C^{(\infty)}(\delta, d; c) = C_{th} \tag{24}$$

in the parameter space. The threshold value  $C_{th}$  must be interpreted as a desired contrast value between the two peaks so that the image resolution is considered to be acceptable. Such parametric curves have the explicit expression

$$d(\delta; c) = \sqrt{\frac{|\delta|}{k}} c \left[ \frac{c^2}{4 \log(C_{th}/2)} - 1 \right]^{-1}, \tag{25}$$

showing the same NA-independent square root trend already demonstrated theoretically for broadening and experimentally demonstrated for complex samples. The dashed curve in Figure 2 shows that Equation (25) correctly predicts the mechanism of the loss of contrast between the two local maxima: the square root trend perfectly reproduces the boundary of the high-contrast region, detaching from it only in very close proximity of focus, where the performance of coherent imaging is defined by the Airy disk.

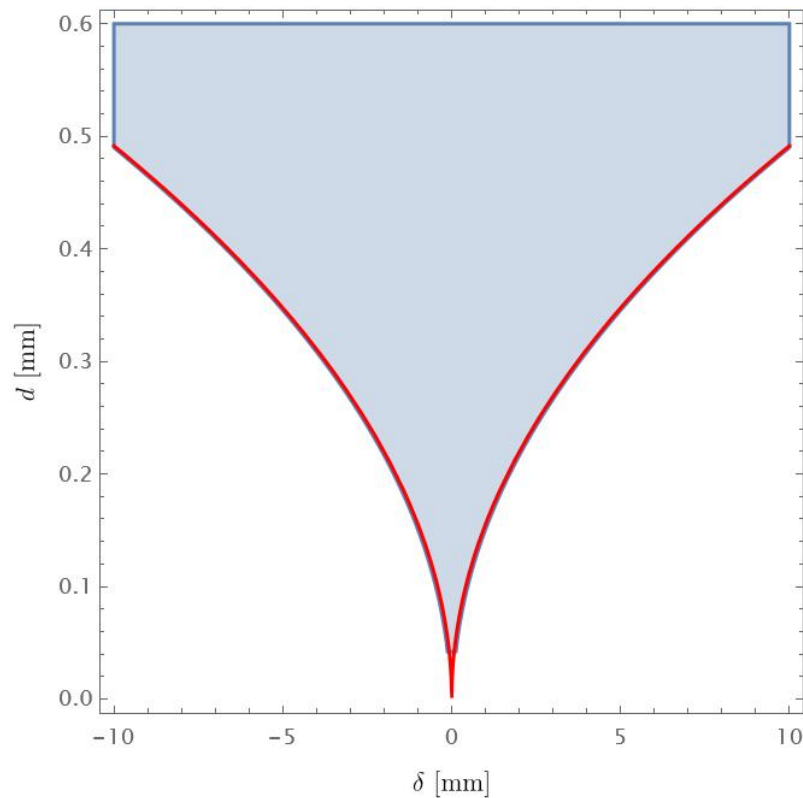


**Figure 2.** The light blue area represents the region where the coherent images of the two Gaussian slits are resolvable in the sense of the contrast criterion for an arbitrarily chosen contrast threshold of 20. The boundary of this region is a curve representing the resolution limit of coherent imaging for the given threshold. The red curve represents the approximated resolution limit curve derived under the assumption of an infinite NA. The two curves almost perfectly overlap; the disagreement only occurs near the focus plane, where the NA sets Rayleigh’s limited resolution.



In the context of coherent imaging, where the definition of resolution employed for incoherent systems does not have a formal analogous counterpart, parametric curves such as Equation (25) should by all means be regarded as *resolution curves*. In fact, they indicate what is the minimum object size  $d$  that can be successfully imaged without having to rely on the concept of the PSF or blurring.

Let us now focus on the relevance of the two mechanisms in determining the final image quality. In particular, despite both the broadening and the loss of contrast due to a peak imposing square root scaling to the *resolution*, we aim to investigate the possibility that one process dominates the other. To this end, we shall consider that the intensity distribution of the coherent image in  $x = 0$  will be moved upward because of both the contribution of the relative maximum from the interference term and the broadening of the two Gaussian images. If the interference contribution is neglected, the origin is a local minimum in the image obtained by superimposing the two slit images. Therefore, contrast can be a good image quality estimator even for this case. By defining the contrast in the origin as the ratio between the absolute maximum of a slit image over its value in the origin, we obtain

$$C'(\delta, d; c) = \frac{I_{\text{coh}}^+(M(\delta)d/2)}{2I_{\text{coh}}^+(0)} = C(\delta, d; c); \quad (26)$$

the factor two at the denominator is due to the fact that broadening is symmetrical for the two slits; hence, the origin receives contributions from both images. The expression shows that the loss of contrast due to broadening is exactly the same as the loss of contrast caused by the presence of a local maximum in the interference term. The two processes can thus always be accounted for together.

#### 4. Discussion

The proposed theoretical framework confirms the superior transversal resolution of *direct* coherent imaging systems over incoherent ones under defocused conditions. By applying the contrast criterion, we investigated the resolution of two Gaussian slits within the coherent imaging regime, specifically in defocus conditions. The analysis reveals a profound distinction between coherent and incoherent imaging systems. Initially, the criterion was applied to a point-like object to establish an analogy with the point-spread function (PSF) in incoherent imaging. As anticipated, in coherent imaging, the PSF loses its physical relevance and cannot reliably estimate the resolution. Subsequently, attention was directed toward applying the contrast criterion effectively to coherent imaging for a two-slit object. By means of the contrast criterion, we were able to define a coherent system analogous to the concept of *resolution curves* for defocused coherent imaging systems without having to rely on the concepts of blurring and the PSF, as is conventionally performed in incoherent techniques (e.g., the Rayleigh limit) [38,39,68].

The presented approach confirmed the established square root scaling law of resolution with defocusing distance in coherent systems. It also uncovered a dual mechanism contributing to contrast loss: the broadening of individual object features leading to overlap and the emergence of mutual interference contributions between object features, peaking midway between them. Remarkably, these two contributions are of comparable magnitude and exhibit consistent scaling behavior.

This work thus really strengthens the evidence that the square root trend of the transverse resolution demonstrated in other related papers (Refs. [34,38,39], for instance) neither depends on the image quality assessment modality nor on the class of objects chosen for testing. In fact, we demonstrated the two mechanisms concurring to image degradation of a double-slit object, observed through a defocused coherent imaging system (i.e., slit broadening and two-slit interference), both resulting in a square root scaling of the resolution as prescribed by diffraction.

An additional key insight is the independence of this scaling law from the numerical aperture (NA), in the case of coherent systems. This contrasts sharply with incoherent imaging systems, both intensity- and correlation-based, where a linear trade-off between res-

olution and depth of field (DOF) limits performance. In coherent imaging, the decoupling of lateral resolution from NA, in defocused imaging conditions, opens new possibilities for high-resolution, scanning-free 3D imaging with high-NA systems. This capability offers a promising avenue for advancing imaging technologies in both fundamental research and practical applications.

**Author Contributions:** Conceptualization and methodology, G.M.; validation, F.V.P. and M.D.; data curation, S.d.G. and A.B.; writing—original draft preparation, G.M., S.d.G. and A.B.; writing—review and editing, G.M., S.d.G., A.B., F.V.P. and M.D.; funding acquisition, M.D. All authors have read and agreed to the published version of the manuscript.

**Funding:** This research was funded by Università degli Studi di Bari under PNRR MUR project no. PE0000023-NQSTI (the National Quantum Science and Technology Institute) and the QUISS Project, financed by INFN.

**Data Availability Statement:** Data are contained within the article.

**Conflicts of Interest:** The authors declare no conflicts of interest.

### Abbreviations

The following abbreviations are used in this manuscript:

NA	Numerical aperture
DOF	Depth of field
CoC	Circle of confusion
CHI	Correlation Hyperspectral Imaging
CPI	Correlation plenoptic imaging
PSF	Point-spread function

### Appendix A

The analytical expressions of the quantities introduced in Equations (11)–(13) are reported below:

$$\sigma_{\text{coh}}^2(\delta, \sigma) = \frac{1}{2} \left( \frac{o}{k\sigma_l} \right)^2 + \frac{2\delta^2\sigma_l^2 + o^2\sigma^2 + 2k^2\sigma_l^2\sigma^4}{(o + \delta)^2 + 2k^2\sigma_l^2\sigma^2 + k^2\sigma^4}$$

$$\sigma_{\text{cross}}^2(\delta, \sigma) = \frac{o^4 + 2o^3\delta + (o^2 + 4k^2\sigma_l^4)\delta^2 + 4o^2k^2\sigma_l^2\sigma^2 + (4k^2\sigma_l^4 + o^2)k^2\sigma^4}{2k^2\sigma_l^2[(o + \delta)^2 + k^2\sigma^2(\sigma^2 + 2\sigma_l^2)]}$$

$$\phi^2(\delta, \sigma) = \frac{2[o^4 + 2o^3\delta + (o^2 + 4k^2\sigma_l^4)\delta^2 + 4o^2k^2\sigma_l^2\sigma^2 + (o^2 + 4k^2\sigma_l^2)k^2\sigma^4]}{k^2[(2\sigma_l^2 + \sigma^2)o^2 + 4k^2\sigma_l^4\sigma^2]}$$

$$\kappa(\delta, \sigma, d) = \frac{2dk^3\sigma_l^2x(o\sigma^2 - 2\delta\sigma_l^2)}{4k^2\sigma_l^4(\delta^2 + k^2\sigma^4) + o^2[k^2\sigma^4 + (\delta + o)^2] + 4k^2o^2\sigma^2\sigma_l^2}$$

### References

1. Garrison, J.; Chiao, R. *Quantum Optics*; Oxford University Press: Oxford, UK, 2008.
2. Walls, D.; Milburn, G. *Quantum Optics*, 2nd ed.; Springer: Berlin/Heidelberg, Germany, 2008.
3. Brida, G.; Genovese, M.; Ruo Berchera, I. Experimental realization of sub-shot-noise quantum imaging. *Nat. Photonics* **2010**, *4*, 227–230. [[CrossRef](#)]
4. Samantaray, N.; Ruo Berchera, I.; Meda, A.; Genovese, M. Realization of the first sub-shot-noise wide field microscope. *Light. Sci. Appl.* **2017**, *7*, e17005. [[CrossRef](#)]
5. Boto, A.N.; Kok, P.; Abrams, D.S.; Braunstein, S.L.; Williams, C.P.; Dowling, J.P. Quantum Interferometric Optical Lithography: Exploiting Entanglement to Beat the Diffraction Limit. *Phys. Rev. Lett.* **2000**, *85*, 2733–2736. [[CrossRef](#)]
6. Dowling, J.P. Quantum optical metrology—the lowdown on high-N00N states. *Contemp. Phys.* **2008**, *49*, 125–143. [[CrossRef](#)]

7. D'Angelo, M.; Chekhova, M.V.; Shih, Y. Two-Photon Diffraction and Quantum Lithography. *Phys. Rev. Lett.* **2001**, *87*, 013602. [[CrossRef](#)]
8. Giovannetti, V.; Lloyd, S.; Maccone, L. Advances in quantum metrology and imaging. *Nat. Photonics* **2009**, *5*, 222–229. [[CrossRef](#)]
9. Moreau, P.A.; Toninelli, E.; Gregory, T.; Padgett, M.J. Imaging with quantum states of light. *Nat. Rev. Phys.* **2019**, *1*, 367–380. [[CrossRef](#)]
10. Schwartz, O.; Levitt, J.M.; Tenne, R.; Itzhakov, S.; Deutsch, Z.; Oron, D. Superresolution microscopy with quantum emitters. *Nano Lett.* **2013**, *13*, 5832–5836. [[CrossRef](#)]
11. Ono, T.; Okamoto, R.; Takeuchi, S. An entanglement-enhanced microscope. *Nat. Commun.* **2013**, *4*, 2426. [[CrossRef](#)]
12. Ekert, A.; Macchiavello, C. Direct characterization of quantum dynamics. *Phys. Rev. Lett.* **2002**, *88*, 217901. [[CrossRef](#)]
13. Clark, A.S.; Chekhova, M.; Matthews, J.C.; Rarity, J.G.; Oulton, R.F. Special Topic: Quantum sensing with correlated light sources. *Appl. Phys. Lett.* **2021**, *118*, 060401. [[CrossRef](#)]
14. Treps, N.; Laurent, C. Quantum imaging with squeezed light. *J. Opt. Soc. Am. B* **2013**, *30*, 29–37.
15. Vahlbruch, H.; Mehmet, M.; Danzmann, K.; Schnabel, R. Detection of 15 dB squeezed states of light and their application for the absolute calibration of photoelectric quantum efficiency. *Phys. Rev. Lett.* **2016**, *117*, 110801. [[CrossRef](#)]
16. Treps, N.; Andersen, U.L.; Buchler, B.C.; Lam, P.K.; Maître, A.; Bachor, H.A.; Fabre, C. Quantum noise in multi-pixel light beams: Spatial squeezing and applications in high-resolution and quantum imaging. *Phys. Rev. Lett.* **2002**, *88*, 203601. [[CrossRef](#)] [[PubMed](#)]
17. Polino, E.; Valeri, M.; Spagnolo, N.; Sciarrino, F. Photonic quantum metrology. *AVS Quantum Sci.* **2020**, *2*, 024703. [[CrossRef](#)]
18. Pittman, T.B.; Shih, Y.H.; Strekalov, D.V.; Sergienko, A.V. Optical imaging by means of two-photon quantum entanglement. *Phys. Rev. A* **1995**, *52*, R3429–R3432. [[CrossRef](#)] [[PubMed](#)]
19. Shih, Y. Quantum imaging. *IEEE J. Sel. Top. Quantum Electron.* **2007**, *13*, 1016–1030. [[CrossRef](#)]
20. Chen, X.; Liu, J.; Luo, K.H.; Wu, L.A.; Zhai, G.J. High-visibility and high-resolution pseudothermal ghost imaging with small laser beam sources. *Opt. Express* **2010**, *18*, 10579–10586.
21. Fu, Y.; Zhang, L.; Chen, X. A review of ghost imaging and its advancements: Innovation and applications. *Adv. Phys. X* **2018**, *3*, 1481262.
22. Valencia, A.; Scarcelli, G.; D'Angelo, M.; Shih, Y. Two-Photon Imaging with Thermal Light. *Phys. Rev. Lett.* **2005**, *94*, 063601. [[CrossRef](#)] [[PubMed](#)]
23. Padgett, M.; Boyd, R.W. An Introduction to Ghost Imaging: Quantum and Classical. *Philos. Trans. R. Soc. A Math. Phys. Eng. Sci.* **2017**, *375*, 20160233. [[CrossRef](#)] [[PubMed](#)]
24. Shapiro, J.; Boyd, R. The physics of ghost imaging. *Quantum Inf. Process.* **2012**, *11*, 949–993. [[CrossRef](#)]
25. Paniate, A.; Massaro, G.; Avella, A.; Meda, A.; Pepe, F.V.; Genovese, M.; D'Angelo, M.; Ruo-Berchera, I. Light-field ghost imaging. *Phys. Rev. Appl.* **2024**, *21*, 024032. [[CrossRef](#)]
26. Gatti, A.; Brambilla, E.; Bache, M.; Lugiato, L. Correlated imaging, quantum and classical. *Phys. Rev. A* **2004**, *70*, 013802. [[CrossRef](#)]
27. Brida, G.; Chekhova, M.; Fornaro, G.; Genovese, M.; Lopaeva, E.; Berchera, I.R. Systematic analysis of signal-to-noise ratio in bipartite ghost imaging with classical and quantum light. *Phys. Rev. A* **2011**, *83*, 063807. [[CrossRef](#)]
28. Bennink, R.S.; Bentley, S.J.; Boyd, R.W. “Two-photon” coincidence imaging with a classical source. *Phys. Rev. Lett.* **2002**, *89*, 113601. [[CrossRef](#)] [[PubMed](#)]
29. Ferri, F.; Magatti, D.; Lugiato, L.; Gatti, A. Differential ghost imaging. *Phys. Rev. Lett.* **2010**, *104*, 253603. [[CrossRef](#)]
30. D'Angelo, M.; Pepe, F.V.; Garuccio, A.; Scarcelli, G. Correlation Plenoptic Imaging. *Phys. Rev. Lett.* **2016**, *116*, 223602. [[CrossRef](#)]
31. Massaro, G.; Giannella, D.; Scagliola, A.; Di Lena, F.; Scarcelli, G.; Garuccio, A.; Pepe, F.V.; D'Angelo, M. Light-field microscopy with correlated beams for high-resolution volumetric imaging. *Sci. Rep.* **2022**, *12*, 16823. [[CrossRef](#)] [[PubMed](#)]
32. Massaro, G.; Mos, P.; Vasiukov, S.; Di Lena, F.; Scattarella, F.; Pepe, F.V.; Ulku, A.; Giannella, D.; Charbon, E.; Bruschini, C.; et al. Correlated-photon imaging at 10 volumetric images per second. *Sci. Rep.* **2023**, *13*, 12813. [[CrossRef](#)]
33. Giannella, D.; Massaro, G.; Stoklasa, B.; D'Angelo, M.; Pepe, F.V. Light-field imaging from position-momentum correlations. *Phys. Lett. A* **2024**, *494*, 129298. [[CrossRef](#)]
34. Massaro, G. Assessing the 3D resolution of refocused correlation plenoptic images using a general-purpose image quality estimator. *Eur. Phys. J. Plus* **2024**, *139*, 727. [[CrossRef](#)]
35. Saleh, B.E.A.; Teich, M.C., Statistical Optics. In *Fundamentals of Photonics*; John Wiley & Sons, Ltd.: Hoboken, NJ, USA, 1991; Chapter 10, pp. 342–383. [[CrossRef](#)]
36. Massaro, G. Analytical form of the refocused images from correlation plenoptic imaging. *Opt. Express* **2024**, *32*, 35755–35770. [[CrossRef](#)]
37. Stokseth, P.A. Properties of a Defocused Optical System. *J. Opt. Soc. Am.* **1969**, *59*, 1314–1321. [[CrossRef](#)]
38. Massaro, G.; Barile, B.; Scarcelli, G.; Pepe, F.V.; Nicchia, G.P.; D'Angelo, M. Direct 3D Imaging through Spatial Coherence of Light. *Laser Photonics Rev.* **2024**, *18*, 2301155. [[CrossRef](#)]
39. Massaro, G.; D'Angelo, M. Characterization of Defocused Coherent Imaging Systems with Periodic Objects. *Sensors* **2024**, *24*, 6885. [[CrossRef](#)] [[PubMed](#)]
40. Massaro, G.; Scala, G.; D'Angelo, M.; Pepe, F.V. Comparative analysis of signal-to-noise ratio in correlation plenoptic imaging architectures. *Eur. Phys. J. Plus* **2022**, *137*, 1123. [[CrossRef](#)]

41. Erkmen, B.I.; Shapiro, J.H. Signal-to-noise ratio of Gaussian-state ghost imaging. *Phys. Rev. A At. Mol. Opt. Phys.* **2009**, *79*, 023833. [[CrossRef](#)]
42. Erkmen, B.I.; Shapiro, J.H. Ghost imaging: From quantum to classical to computational. *Adv. Opt. Photonics* **2010**, *2*, 405–450. [[CrossRef](#)]
43. Lugiato, L.; Gatti, A.; Brambilla, E. Quantum imaging. *arXiv* **2002**, arXiv:quant-ph/0203046. [[CrossRef](#)]
44. O’Sullivan, M.N.; Chan, K.W.C.; Boyd, R.W. Comparison of the signal-to-noise characteristics of quantum versus thermal ghost imaging. *Phys. Rev. A At. Mol. Opt. Phys.* **2010**, *82*, 053803. [[CrossRef](#)]
45. Favaro, P.; Mennucci, A.; Soatto, S. Observing shape from defocused images. *Int. J. Comput. Vis.* **2003**, *52*, 25–43. :1022366408068 [[CrossRef](#)]
46. Wu, G.; Masia, B.; Jarabo, A.; Zhang, Y.; Wang, L.; Dai, Q.; Chai, T.; Liu, Y. Light field image processing: An overview. *IEEE J. Sel. Top. Signal Process.* **2017**, *11*, 926–954. [[CrossRef](#)]
47. Ihrke, I.; Restrepo, J.; Mignard-Debise, L. Principles of Light Field Imaging: Briefly revisiting 25 years of research. *IEEE Signal Process. Mag.* **2016**, *33*, 59–69. [[CrossRef](#)]
48. Georgiev, T.; Lumsdaine, A. The multifocus plenoptic camera. In *Digital Photography VIII*; Battiato, S., Rodricks, B.G., Sampat, N., Imai, F.H., Xiao, F., Eds.; Society of Photo-Optical Instrumentation Engineers (SPIE) Conference Series; SPIE: Bellingham, WA, USA, 2012; Volume 8299, p. 829908. [[CrossRef](#)]
49. Massaro, G.; Pepe, F.V.; D’Angelo, M. Correlation Hyperspectral Imaging. *Phys. Rev. Lett.* **2024**, *133*, 183802. [[CrossRef](#)] [[PubMed](#)]
50. Ralston, T.S.; Marks, D.L.; Carney, P.S.; Boppart, S.A. Interferometric synthetic aperture microscopy. *Nat. Phys.* **2007**, *3*, 129–134. [[CrossRef](#)]
51. Tian, L.; Wang, J.; Waller, L. 3D differential phase-contrast microscopy with computational illumination using an LED array. *Opt. Lett.* **2014**, *39*, 1326–1329. [[CrossRef](#)]
52. Tian, L.; Waller, L. 3D intensity and phase imaging from light field measurements in an LED array microscope. *Optica* **2015**, *2*, 104–111. [[CrossRef](#)]
53. Gabor, D. Microscopy by reconstructed wave-fronts. *Proc. R. Soc. A* **1949**, *197*, 454–487. [[CrossRef](#)]
54. Ferraro, P.; Wax, A.; Zalevsky, Z. *Coherent Light Microscopy: Imaging and Quantitative Phase Analysis*; Springer: Berlin/Heidelberg, Germany, 2011. [[CrossRef](#)]
55. Osten, W.; Faridian, A.; Gao, P.; Körner, K.; Naik, D.; Pedrini, G.; Singh, A.K.; Takeda, M.; Wilke, M. Recent advances in digital holography. *Appl. Opt.* **2014**, *53*, G44–G63. [[CrossRef](#)]
56. Zheng, G.; Horstmeyer, R.; Yang, C. Wide-field, high-resolution Fourier ptychographic microscopy. *Nat. Photonics* **2013**, *7*, 739–745. [[CrossRef](#)] [[PubMed](#)]
57. Rodenburg, J.; Maiden, A. Ptychography. In *Springer Handbook of Microscopy*; Springer International Publishing: Berlin/Heidelberg, Germany, 2019; pp. 819–904. [[CrossRef](#)]
58. Zheng, G.; Shen, C.; Jiang, S.; Song, P.; Yang, C. Concept, implementations and applications of Fourier ptychography. *Nat. Rev. Phys.* **2021**, *3*, 207–223. [[CrossRef](#)]
59. Horstmeyer, R.; Ou, X.; Zheng, G.; Willems, P.; Yang, C. Digital pathology with Fourier ptychography. *Comput. Med. Imaging Graph.* **2015**, *42*, 38–43. [[CrossRef](#)] [[PubMed](#)]
60. Patra, D.; Gregor, I.; Enderlein, J.; Sauer, M. Defocused imaging of quantum-dot angular distribution of radiation. *Appl. Phys. Lett.* **2005**, *87*, 101103. [[CrossRef](#)]
61. Patra, D.; Gregor, I.; Enderlein, J. Image Analysis of Defocused Single-Molecule Images for Three-Dimensional Molecule Orientation Studies. *J. Phys. Chem. A* **2004**, *108*, 6836–6841. [[CrossRef](#)]
62. di Francia, G.T. Resolving Power and Information. *J. Opt. Soc. Am.* **1955**, *45*, 497–501. [[CrossRef](#)]
63. Scattarella, F.; Massaro, G.; Stoklasa, B.; D’Angelo, M.; Pepe, F.V. Periodic patterns for resolution limit characterization of correlation plenoptic imaging. *Eur. Phys. J. Plus* **2023**, *138*, 710. [[CrossRef](#)]
64. Wani, P.; Usmani, K.; Javidi, B. Generalization of the two-point-source resolution criterion in the presence of noise. *Opt. Lett.* **2023**, *48*, 4009–4012. [[CrossRef](#)] [[PubMed](#)]
65. Diffraction and Interference in Image Formation. In *Fundamentals of Light Microscopy and Electronic Imaging*; John Wiley & Sons, Ltd.: Hoboken, NJ, USA, 2012; Chapter 5, pp. 79–101. [[CrossRef](#)]
66. Tan, W.; Huang, X.; Jiang, T.; Nan, S.; Fu, Q.; Zou, X.; Bai, Y.; Fu, X. Critical resolution in ghost imaging system with pseudo-thermal light. *Results Phys.* **2022**, *32*, 105104. [[CrossRef](#)]
67. Goodman, J.W. *Introduction to Fourier Optics*, 3rd ed.; Goodman, J.W., Ed.; Roberts & Co.: Englewood, CO, USA, 2005.
68. Aert, S.V.; Dyck, D.V.; den Dekker, A.J. Resolution of coherent and incoherent imaging systems reconsidered— Classical criteria and a statistical alternative. *Opt. Express* **2006**, *14*, 3830–3839. [[CrossRef](#)]

**Disclaimer/Publisher’s Note:** The statements, opinions and data contained in all publications are solely those of the individual author(s) and contributor(s) and not of MDPI and/or the editor(s). MDPI and/or the editor(s) disclaim responsibility for any injury to people or property resulting from any ideas, methods, instructions or products referred to in the content.